Application of in-situ liquid cell transmission electron microscopy in corrosion studies a critical review of challenges and achievements

Kosari, Ali; Zandbergen, Henny; Tichelaar, Frans; Visser, Peter; Terryn, Herman; Mol, Arjan

DOI
10.5006/3369

Publication date
2020

Document Version
Accepted author manuscript

Published in
Corrosion

Application of in-situ liquid cell transmission electron microscopy in corrosion studies: a critical review of challenges and achievements

Ali Kosari*, Henny Zandbergen**, Frans Tichelaar**, Peter Visser***, Herman Terryn**** and Arjan Mol†*

Keywords:

Aqueous corrosion
In-situ liquid cell TEM
Initiation events
Electron beam effect
Specimen preparation
(S)TEM imaging mode

** Department of Materials Science and Engineering, Delft University of Technology, Mekelweg 2, 2628 CD Delft, The Netherlands*

*** Kavli Institute of Nanoscience, Delft University of Technology, Lorentzweg 1, 2628 CJ Delft, The Netherlands*

**** AkzoNobel, Rijksstraatweg 31, 2171 AJ, Sassenheim, The Netherlands*

***** Department of Materials and Chemistry, Research Group Electrochemical and Surface Engineering (SURF), Vrije Universiteit Brussel, Pleinlaan 2, 1050 Brussels, Belgium*

† Corresponding author: Email: J.M.C.Mol@tudelft.nl.

ABSTRACT

Identifying corrosion initiation events in metals and alloys demands techniques that can provide temporal and spatial resolution simultaneously. Transmission electron microscopy (TEM) enables to obtain microstructural and chemical descriptors of materials at atomic/nanoscopic level and has been used in corrosion studies of many metal-electrolyte combinations. Conventionally, ex-situ and quasi in-situ TEM studies of pre- and post-corroded samples were performed, but possible experimental artefacts such as dehydrated surfaces might not fully represent the real interfacial conditions as compared to those when actually immersed in the electrolyte. Recent advances in liquid cell transmission electron microscopy (LC-TEM) allows for in-situ monitoring morphological and even compositional evolutions in materials resulting from interaction with gas or liquid environments. Corrosion science, as a challenging field of research, can benefit from this unparalleled opportunity to investigate many complicated corroding systems in aqueous environments at high resolution. However, 'real life' corrosion with LC-TEM is still not straightforward in implementation and there are limitations and challenging experimental considerations for conducting reliable examinations. Thus, this study has been devoted to discussing the challenges of in-situ LC-TEM whereas state-of-the-art achievements in the field of relevance are reviewed.

INTRODUCTION

Detailed understanding of local corrosion events and processes in alloys at very early stages of exposure to a corrosive environment are of pivotal importance to developing timely and effective inhibition strategies to avoid premature failures [1, 2]. Techniques to probe corrosion initiation are limited where concurrent chemical, electrochemical and morphological characterizations at a high resolution are essential [3-5]. That is why theories have traditionally been established through bridging and linking information obtained from separately performed experiments involving multiple techniques [6-8]. Transmission electron microscopy (TEM) can provide information at atomic resolution that can be correlated to a structure, morphology, and composition of an object directly [9] (Fig. 1). However, due to limiting factors such as a thin object size (5-300 nm) and the vacuum operating conditions, practical TEM corrosion studies were ex-situ typically, i.e. after the corrosion event, and of dehydrated surfaces (post-mortem characterizations) [10-16]. Thus, concluding statements are sometimes uncertain and debatable when compared to the real-life conditions since active solid/electrolyte interfaces cannot be evaluated real-time in such ex-situ studies. In addition, ex-situ characterizations, in case of long term studies of alloy corrosion in harsh environments [17, 18], always suffer from the lack of time-resolved information on the degradation kinetics of samples.

As an alternative, quasi in-situ TEM approaches have been applied to corrosion studies recently [19-23]. 'Quasi in-situ' implies that an identical location on a thin sample is exposed intermittently to a corrosive environment outside the microscope and subsequently examined with TEM. Although characterizations still need to be done statically in vacuum, this method has so far delivered valuable insights mainly into early stages of corrosion in many alloys as morphological and chemical evolutions can directly be evidenced at the nanoscale [21]. Nevertheless, there are still potential drawbacks to this approach. For instance, the solution chemistry at sites undergoing localized corrosion attack normally develop differently with time than the bulk solution chemistry. Therefore, these specific sites might never become active again subsequent to the drying process or at least not reach the same conditions over the next rounds of exposure as compared to an undisturbed exposure case. Furthermore, artefacts and particularly carbon contaminations may be introduced into the system during handling and analyzing the specimens, leading to beam-induced carbon depositions which can steer and change the corrosion mechanism and kinetics differently as compared to the uninterrupted exposure case [24].

Nowadays, in-situ TEM can be implemented for corrosion studies by means of thin-window cells which elegantly isolate the specimen and its liquid surrounding from vacuum [25-28]. This development allows for studying morphological and even compositional evolutions of alloy specimens real time and in-situ as a consequence of interaction with corrosive environments at a desired temperature (operando) [29]. This ambition strongly demands optimized experimental conditions for in-situ LC-TEM, that can simultaneously provide a high spatial and temporal resolution [30-34], as initiation processes take place dynamically and relatively fast at the metal/electrolyte interface [35]. In fact, corrosion initiation often occurs at surface heterogeneities where microstructure and composition variations result in electrochemical interaction and reactivity [21, 35-39]. In-situ TEM movies can capture insightful events to understand mechanisms behind local corrosion attack in real specimens exposed to inhibited/uninhibited solutions. Impressively, the samples loaded in electrochemical liquid cells can now be biased externally, whereby local dissolution events can be correlated directly to the corresponding morphological changes [40-43]. This can be utilized to conduct several studies using in-situ LC-TEM to probe dynamic nanoscale phenomena such as transition from metastable events to stable pitting corrosion at the nanoscale in many metallic systems like stainless steels, Al, Ti and Mg alloys [39, 44-51].

Even though LC-TEM provides an unprecedented opportunity of studying many complicated corroding systems at the nanoscopic level, it has raised demanding technical implications and concerns during interpretation of electrochemical events [52-55]. This study discusses limitations and challenges of in-situ LC-TEM applied to aqueous corrosion. Furthermore, noteworthy achievements in the field of relevance are reviewed.

Instrumentation for in-situ LC-TEM

Toward practical liquid phase TEM studies, the recent technological advances have led to the development of dedicated microelectronic mechanical systems (MEMS) and TEM specimen holders [56]. In the contemporary designs, liquid cells are comprised of assembled top and bottom chips by which the liquid can be separated from the TEM column environment [57]. The electron-transparent windows (membranes) are usually made of amorphous Si_xN_y on silicon support substrates; the thickness of membranes usually varies from 20 to 50 nm to reach a balance between mechanical properties and imaging resolution [25]. As a key character that enables electrochemical measurements, Pt electrodes including working (WE), reference (RE) and counter electrodes (CE) can be integrated onto the chips [40] (Fig. 2a). This provides a practical opportunity to apply anodic or cathodic potentials externally by a potentiostat [58]. In addition, a heating resistive pattern can also be designed on the chip to control the solution and sample temperature [59].

In practice, liquid cells (LCs) must be assembled manually in a way that rectangular windows overlap, allowing electron beam transmission through the LC. Si_xN_y membranes are usually hydrophobic as manufactured, repelling water to flow into the liquid cell. To make the membranes hydrophilic, the chips should be treated prior to assembling by either glow discharge or O_2 plasma cleaning. Such treatments are of additional benefit to get rid of carbon contaminations introduced during handling the specimens [55]. Spacers are patterned onto one of the chips to regulate the minimum distance between the top and bottom membranes; they are usually defined to be 150-500 nm tall. Despite the detailed design of the LCs, there will still be bulging of thin membranes when inserted into the high vacuum column, giving rise to higher water thickness than the desired spacing [60, 61]. The liquid cell needs to be leak-tight and this usually can be fulfilled either by gluing the cell or using sealing O-rings [62]. The assembled cell is placed on the specific TEM holder that can convey liquid to the inlet through a tubing system (Fig. 2b and c). To mitigate carbon deposition on the samples and membranes while illuminating the liquid cell, the solutions should be filtered to remove long hydrocarbon molecules in the solutions. In a prepared liquid cell loaded with a thin sample, the electron beam can readily travel through if the total path length is suitably short. In addition, a stagnant or flowing electrolyte is controlled by a syringe or pressure-based pump. Although the interaction of electrons with LC components can be used for dynamically recording and analysis of the specimen evolution with exposure, it might give rise to electrolyte radiolysis (Fig. 2d). In fact, the electron-beam effect is the main challenge of in-situ LC-TEM and must be well considered and understood to avoid any erroneous conclusion [53, 54, 63].

Challenges of LC-TEM

Since the advent of the liquid phase TEM, image resolution and electron beam effect have been addressed as two major challenging factors [63, 64]. Furthermore, specimen preparation from the material to be studied and the transfer process can be considered as additional challenging issues during which the specimens are cut out of a 'region of interest' and positioned onto the fragile membranes.

Specimen preparation and transfer to liquid cells

One of the most crucial and time-consuming stages of the liquid cell setup is to delicately place a thin TEM specimen over the brittle windows necessarily with a micron range precision. This should be done precisely otherwise even hairline damages to the membrane during transfer may lead to failure of the liquid cell during the operation in the high vacuum of a TEM column. As an added challenge, the overall thickness of specimens must fit within a 100-500 nm distance determined by spacers. Amongst conventional techniques, Ga^+ focused ion beam (FIB) preparation has been popular as thin specimens (lamellae) can selectively be fabricated out of 'regions of interest' in real bulk metals/alloys [65, 66]. In the case of liquid cells, a specific site is milled down to electron transparency. Next, the lamella is extracted from the trench and positioned on the chip either with ex-situ micro-manipulators under a light microscope, or with in-situ internal nano-manipulators installed on the FIB machines [67]. Reported as a drawback, Ga^+ ions can be implanted into the lamellae surface during ion sputtering and thinning; this phenomenon can induce structural and compositional surface modifications according to the primary ion-beam energy [67, 68]. Since corrosion initiation events are highly dependent on surface heterogeneities, a final cleaning process using a low-energy ion beam should be performed to mitigate Ga^+ ion impact and avoid probable erroneous conclusions. In addition, the Pt overlays, normally deposited to protect the top part of lamella from Ga damage, can be an issue when the specimen is in contact with an aqueous electrolyte, providing a galvanic couple with the region of interest.

Taking into account these concerns, a hybrid sample preparation procedure dedicated to liquid cells has recently been established [69, 70]. In this methodology, which is comprised of three basic steps, electropolished TEM thin-foil disks are initially prepared. Then, the region of interest is selected from an electron transparent area, followed by cutting it from the disk. Next, the plan-view section is lifted, positioned and finally fixed to the liquid cell using a FIB/SEM machine (see steps in Fig. 3). However, electropolished specimens are not recommended for corrosion studies as the samples undergo a pre-corrosion process during electropolishing, especially in the case of alloys prone to dealloying [71, 72]. As an alternative, Ar ion-milled specimens are more favored in LC-TEM corrosion studies.

Illumination modes and specimen configurations

Two illumination modes are available for in-situ LC-TEM corrosion studies: TEM and STEM. In both modalities, the image resolution is degraded by the multiple scattering of electrons in the liquid which depends strongly on the position of the specimen relative to the enclosing membranes of the LC [25, 64], although it is also limited by the specifications of the employed microscope like acceleration voltage, detectors, cameras, spherical and chromatic aberrations [55, 73-75]. Since the specimen must be attached to one of the membranes two possibilities exist: the specimen is positioned at the top or entrance membrane where the electron beam enters the LC, or the specimen is positioned at the bottom, or exit membrane. The dependency of image resolution for both imaging modes on these locations is called the top-bottom effect [52], and is illustrated in Fig. 4 for a corroded part of an AA2024-T3 alloy.

In TEM mode, a better resolution is achieved when the specimen is close to the beam exit side of the liquid cell (see Fig. 4a and b); the corrosion features and intermetallic phases are well distinguishable. The reason is that any further elastic scattering of electrons in the electrolyte between the exit membrane and the specimen generates

additional blurring [25]. Thus, in TEM mode, the objects further from the exit side of the liquid layer are imaged with poorer resolution. Comparatively, in STEM mode, the highest resolution is acquired when the specimen is placed on the top chip (at the entrance side of the beam). In STEM mode, image resolution is highly determined by the probe diameter; however, the beam progressively undergoes broadening while passing through the liquid cell as a result of multiple scattering [76]. For optimizing an in-situ corrosion study, the specimen needs to be as bulk-like as possible, i.e. relatively thick samples are preferred. For such samples, STEM mode is reported to provide better quality of images than TEM, in particular, bright field STEM where beam broadening effect is less critical because of the detector characteristics [77]. In addition, annular dark field STEM, which, depending on the camera length, can be quite sensitive to differences in the atomic number (Z) of atoms and even diffraction contrasts within the specimen, has the benefit of showing Z-contrast and local thickness information more clearly. However, the spatial resolution is typically limited to the signal-to-noise ratio (SNR). This is observed in Fig. 4 in which dispersoids phases in AA2024-T3 matrix and localized attacks are well revealed with ADF-STEM. The detailed information about optimization of the parameters like dose rate, detectors etc. for STEM imaging can be found in the recent paper published by De Jonge [77].

In contemporary liquid cells, the gap between the top and bottom chips is controlled by the height of the spacers. However, when the liquid cell is introduced into a high vacuum area, the pressure difference between the inside and the outside of the cell leads to an outward bowing of the membranes (bulging effect) [57]. As schematically depicted in Fig. 5a, the liquid thickness increases considerably from the edges toward the center of the membrane, highly depending on the window width and membrane thickness. As an example, for 40-µm-wide membranes that are orthogonally oriented to each other and gapped with 500-nm-tall spacers, the bulging varies across the membrane from almost zero around the corners to approx. 500 nm in the center [78]. It is worth noting that electron energy loss spectroscopy (EELS) enables to estimate the thickness of the liquid layer in terms of the mean free path based on the primary electron beam energy [79]. Thus, as a practical note, the lamella should be positioned close to the edges where the degree of bowing is smallest. Fig. 5b shows the spatial resolution in TEM and STEM to be strongly dependent of the liquid thickness; it is theoretically estimated for imaging Au nanoparticles [25]. According to the plot, the resolution in STEM is less dependent on the liquid thickness, as compared to TEM. This fact supports the STEM mode to be used in corrosion studies in which a wider range of possible electrolyte thicknesses is preferred to allow various and possibly varying realistic atmospheric corrosion conditions to be studied.

The effects of electron beam on solution chemistry

Radiolysis occurs when electrons travelling through a liquid cell interact with water molecules, delivering energy to the irradiated region mostly as a consequence of inelastic scattering of electrons [80]. While the transferred energy slightly heats the liquid cell, it may also convert water molecules and its constitutive atoms into various radical species like hydrated electrons eh^-, hydrogen radicals $H^\bullet$, hydroxyl radicals $OH^\bullet$ and more as follows [63]:

$$H_2O \rightarrow eh^-, H^\bullet, OH^\bullet, H_2, H_2O_2, H_3O^+, HO_2^\bullet$$

TEM and STEM imaging are performed typically at dose rates of 10^5–10^7 Gy s^{-1}, providing steady-state concentrations of the aqueous radicals [81, 82]. Therefore, the illuminated volume may suffer from a different local chemistry, in particular pH, highly dependent on the beam energy and intensities. For de-aerated water, the steady state pH is a function of dose rate and initial pH [82]. As shown in Fig. 6, the pH of the solution is less affected by irradiation at very low dose rates; acidic solutions do not or only at relatively high dose rates change their pH whereas alkaline solutions might get more acidic in the presence of the beam. Compared to aerated solutions, the electron beam can produce a slightly higher concentration of H^+ in initially moderate pH ($5 < pH < 9$) neutral solutions and almost equal in acidic and basic environments. In addition, other radicals are of particular importance since the hydrated electrons (eh^-) and the hydrogen radicals $H^\bullet$ as strong reducing species and hydroxyl radicals $OH^\bullet$ as strong oxidizing agent can interact with the specimens [81]. Thus, it would be beneficial to deliberately add species that scavenge radicals, mitigating their impact on solution chemistry; a list of possible scavengers for various radicals are listed by Woehl and Abellan [81].

In TEM and STEM imaging modes, the electron beams pass the aqueous electrolyte in different configurations. In STEM illumination, point excitation occurs while rastering the focused electron probe over the liquid cell at each scan point, generating local radical concentrations highly dependent on the pixel dwell time and magnification. In opposite, a broad static beam in TEM imaging continuously irradiates the specimen, typically delivering a higher cumulative dose rate than STEM. For quick dynamic processes, TEM imaging is capable of fast capturing although it often gives rise to bubbling [80]. Furthermore, the energy of the incident electrons can affect the delivered dose rate to the liquid cell; the higher accelerating voltages (i.e. 300 keV) are observed to create less radicals owing to lower electron stopping power in water [83]. In reality, the liquid cells are not uniform in terms of geometry and materials, thus there would be a spatial variation in dose rate due to a varying exchange of dose at the solid/liquid interface. In fact, secondary and backscattered electrons emitted out of the membranes and specimens, which have higher atomic number and density than water, can also contribute to the total dose rate. This phenomenon can increase the dose rate by several times within nanometric proximity of, for example, a water/electrode interface [84].

Regarding corrosion studies, the solution chemistry is of critical importance as it can modify dissolution events and passive surface layers. In fact, corrosion of many alloys is highly pH dependent; for instance, passive layers are undermined in acidic solutions where aggressive species like chloride may readily cause breakdown of the protective surface layers [37, 38, 85-87]. In addition, formation of species like $Cl^\cdot$, $Cl_2^{\cdot-}$ and $HClO^{\cdot-}$ [88] are plausible which add to other oxidizing species like H_2O_2 and O_2 formed by water radiolysis, although Cl^- is reported to be $OH^\bullet$ and $H^\bullet$ scavenger in acidic solutions [81]. The electron beam effect is even more pronounced for corrosion inhibitor-containing solutions as some inhibitor molecules respond differently to pH variations where they can form local deposits over local anodes and cathodes [89]. For example, cerium-based compounds are known as cathodic inhibitors which can deposit a protective layer based on local alkalinity [90, 91]. On the other hand, inhibited systems with reducible species like cerium ions can undergo beam-induced deposition through reduction reactions with hydrated electrons or hydrogen radicals. In such systems, TEM mode imaging is preferred [92] as STEM illumination can generate a large local radical concentration by point excitation to the liquid at each scan point, providing a high local threshold electron dose for reduction nucleation [93]. Thus, the electron beam effect and imaging mode should be well considered otherwise the mechanisms observed would be misunderstood with LC-TEM. As a straightforward approach, lowering the dose rate can highly reduce the beam effect, however it induces noise on images and as a consequence a lower temporal resolution in LC-TEM. Noise in low-dose imaging is minimized

with the new generation of imaging cameras and direct electron detectors, but can still reduce the spatial resolution, in particular for specimen-loaded liquid cells which are normally thick [75]. It should be noted that the spatial resolution in both TEM and STEM scales with dose rate to the power -1/4. It indicates that even slightly improved resolution would be at the expense of a huge rise of the electron dose, but on the other hand, a large decrease of the electron dose insignificantly affect the resolution [77].

Electrochemical measurements in liquid cells

Nowadays, liquid cells for in-situ TEM are highly developed and can be linked to an external source like a potentiostat for biasing electrochemical reactions at electrode/electrolyte interface while the corresponding morphological evolutions are recorded [41]. The grounding configuration of the potentiostat and microscope is important to diminish noise within the system [94]. Electrochemical data recorded in a liquid cell can be affected by either the thin electrolyte or the electron beam [40]. The former giving rise to a potentially considerable ohmic-drop, and mass-controlled reactions should be managed by smart patterning of a platinum reference electrode quite close to the working electrode and flowing electrolyte, respectively [40]. However, the effect of the electron beam on the electrochemical processes is yet to be understood. Open circuit potential (OCP) measurements are reported to be largely influenced by the beam [94, 95]. Fig. 7b shows variations in the OCP of a Pt electrode recorded when the beam is intermittently blanked or de-blanked; it is excited up to 500mV in the stagnant solution. In comparison, the OCP of an austenitic stainless steel 0.001 M H_2SO_4 is almost unaffected by the beam, particularly when it is approaching the steady state (see Fig. 7c). In fact, the liquid cell configuration can function as a plate capacitor while an electrically conductive electrolyte allows for the exchange of charges, resulting in such behavior; more information can be found in Ref [95]. Interestingly, hysteresis analysis of cyclic voltammetry curves has shown independency of the recorded currents in the presence of the STEM beam scanning over a glassy carbon electrode (see Fig. 7d) [96]. Furthermore, electrochemical impedance spectroscopy (EIS) has revealed the effect of mass-transfer on electrochemical reactions in the liquid cell. As can be seen in Fig. 7e, the low frequency loop related to mass-controlled events gets significantly smaller by increasing the flow rate [96].

The liquid cells are mainly designed for battery or electrodeposition applications which normally are conducted by inert working electrodes like Pt and Au. To conduct electrochemical corrosion evaluations, the alloy specimens need to be electrically connected to the electrode. Since both the specimen and the electrode are in contact with the electrolyte, galvanic coupling may influence and essentially fully disturb the corrosion mechanism and kinetics of the system. Moreover, quasi Pt reference electrodes that are used in liquid cells have a potential highly dependent on the solution chemistry. Thus, before the in-situ LC-TEM measurement, potential measurements should be performed with respect to conventional reference electrodes in bulk-scale to calibrate the potential of the Pt reference electrode in a specific solution chemistry. However, the electron beam can still have an undesirable effect as the solution chemistry can be changed by the beam, causing modifications in the quasi reference electrode potential which cannot be distinguished from real OCP evolutions of the specimen.

Recent achievements of LC-TEM in corrosion science

In recent years, the in-situ LC-TEM has been applied to a variety of research fields; corrosion is also one of the potential fields to take advantage of this opportunity to unravel yet-to-be-resolved aspects in corrosion initiation and inhibition phenomena. Actually, this has just begun in 2013 by investigating localized corrosion of AA2024-T3, albeit in a vapor phase of a HCl/water mixture [97]. However, contemporary liquid cells and holders have paved the way to investigate many complicated corroding systems in liquid. Herein, state-of-the-art achievements of liquid cell TEM investigations in the field of corrosion studies are discussed.

In-situ liquid cell TEM corrosion of metal thin films

Preliminarily works in corrosion science have focused on corrosion of metal thin films due to simplicity of the system; the results of in-situ LC-TEM can be compared with bulk-scale findings [98-102]. In practice, thin films can directly be patterned with conventional techniques onto the chips or even further modified by ion implantations. Real-time morphological evaluations on Cu thin films exposed to a flowing NaCl solution have shown preferential dissolution of individual grains [100]. Preferential attacks to the grains, in particular, adjacent to an abnormally grown grain have been observed in Fe thin films [102]. Time-resolved TEM images, shown in Fig. 8a-f, reveal a high reactivity of grains with high surface area to volume ratio, while the large grain remains unaffected during 25 min exposure to 20% acetic acid. In another interesting study, Al thin films were biased to study their progressive morphological response to polarization with in-situ LC-TEM. Illustrated in Fig. 8g-j, cathodic polarization does not change the morphology while dissolution of individual grains, distinguished as dark regions, is observed in the anodic region of the curve. Recently, dissolution events of thin films are also studied at elevated solution temperatures [101]. Although, metal thin film studies can rarely mimic real-life corrosion of alloys, they are still beneficial to understand the beam impact on dissolution events and radiolysis of solutions with a complex chemistry.

Analytical in-situ liquid TEM of austenitic stainless steel

Stainless steels are very resistive to uniform corrosion but highly susceptible to pitting corrosion [103]. MnS inclusions are mostly liable for pit initiation by releasing sulfur species which can give rise to de-passivation in the presence of chloride [104-106]. Crevice formation at the edge of dissolving inclusions is proposed as a main mechanism of pit nucleation on stainless steels [107, 108]. Therefore, in-situ liquid TEM would be suitable to show evidence of dissolution of MnS inclusions that trigger breakdown of the passive film in chloride containing solutions. Although it is challenging to observe the passive film on a stainless steel in the liquid phase due to limited resolution, progressive dissolution around the inclusions can clearly be observed. In recent years, electrochemical liquid cells equipped with a resistive heater were also developed to investigate pitting corrosion of modern stainless steels with a high pitting potential and critical pitting temperature (CPT) [109].

In a recent study, thin pieces of type 304 stainless steel containing MnS inclusions have been studied with in-situ LC-TEM. Initial chemical and morphological characterizations have been done in 1 bar air, followed by exposing to distilled water for 24 hr [95]. Fig. 9 shows that the dissolution of a specific MnS inclusion takes place as an initial corrosion

event whereas no dissolution of the steel has been observed because of the absence of chloride. However, direct evidence still needs to be provided with in-situ LC-TEM showing an MnS inclusion to induce active dissolution at the adjacent passive region.

Corrosion of low-carbon steel at the nanoscale

Corrosion of plain steel in oil and gas industry is a challenging concern as premature failure occasionally happens due to localized attack highly dependent on the environment [110, 111]. Having studied generally with ex-situ evaluations, insights into dynamic nanoscopic phenomena at heterogeneities are essential to establish models that can fully predict all the uniform and non-uniform corrosion processes [112-114]. In a very interesting paper, it has been shown with in-situ LC-TEM that initiation events can take place at triple junctions formed by cementite confined by ferrite grains [115]. Time-resolved bright field STEM has shown that local dissolution progressively propagates along the cementite/ferrite interface (see Fig. 10b-e) while no further evolution of localized corrosion have been observed during short term exposure. The amount of uniform corrosion in steel has also been evaluated in the lamella before and after exposure to the electrolyte (see Fig. 10g and h). Post-corrosion analysis has been conducted by mapping the relative thickness via an EF-TEM approach, revealing selective dissolution of ferrite neighboring cementite (Fig. 10i). Further support for determining the type of corrosion products has been obtained by EELS analysis, suggesting formation of iron oxide over ferrite grains [115].

Summary and outlook

Promising and exciting years are ahead of us in corrosion science with the rise and availability of in-situ liquid cell TEM to explore many complicated corroding systems. Real thin specimens can be prepared with FIB/SEM techniques or hybrid approaches. However, artefacts like Ga damage which can change the chemical composition of the specimens might be introduced into the system during sample preparation and handling; proper approaches must be selected to alleviate their impact. The specimens can partly be masked with inert materials to restrict corrosion processes to the field of view. Both TEM and STEM can be used in liquid cell imaging; the STEM operation mode is preferred for thick liquid cells whereas the TEM mode provides higher frame rates in imaging videos. When an electrolyte is introduced in the liquid cell, both the resolution and image contrast are considerably decreased; its effect can largely be reduced with a favorable sample position in the LC corresponding to either imaging mode. Minimizing the effect of the electron beam on solution chemistry is crucial to reduce its effect on the corrosion mechanisms and kinetics, in particular for complex solutions. As a direct result of irradiation at high dose rates, the formation of oxidizing radiolytic species might change the solution pH and thus modify the nature and kinetics of corrosion events. In addition, for NaCl solutions, species like $Cl^{\cdot}$, $Cl_2^{\cdot-}$ and $HClO^{\cdot-}$ are possibly formed by radiolysis; therefore, running beam-off experiments, in parallel, is needed to study possible beam influences. The beam effect can be highly diminished by conducting low-dose rate imaging or flowing electrolyte experiments but at the expense of image resolution and corrosion-induced local chemistry, respectively. To conduct electrochemical measurements in liquid cells, alloy specimens must be in contact with noble electrodes like Pt where galvanic corrosion would highly be plausible at contact locations. This requires the design of electrochemical chips with the specific application of corrosion science in mind. Moreover, the potential of quasi Pt reference electrodes is highly dependent on the solution chemistry. They should be patterned away from the irradiated region; however, this would give rise to a higher ohmic drop. Analytical TEM characterizations with EDS and EELS can be done on the post-corroded specimens to gain insights into the type of corrosion products. In the case of uniform corrosion, no significant contrast variation is seen, thus post EF-TEM analysis would be helpful to observe thickness reductions due to the metal dissolution.

In-situ liquid cell TEM has the potential to be applied in a wide range of corrosion studies, however, thickness limitations of specimens make it more appropriate for studying early stage corrosion phenomena. Pitting in many alloy systems like stainless steels, aluminum, titanium and copper alloys are yet to be either understood or evidenced directly to establish mechanisms well explaining the initiation processes. LC-TEM can be utilized to link morphological evolutions and electrochemical responses caused by corrosion. For instance, in an electrochemical liquid cell, morphological changes as a consequence of local attack can produce transient currents that can be recorded externally with a potentiostat. Thus, in-situ LC-TEM, granting a good temporal and spatial resolution can discriminate between stable and metastable processes. In the current stage, it is possible to conduct electrochemical and morphological evaluations of corrosion at desired temperatures. In the future with ongoing technological advancements, it might be even practical to do complicated corrosion studies like mechanically influenced corrosion such as stress corrosion cracking within the liquid cell while beam effects are highly avoided.

Acknowledgement

This work is part of the research programme Understanding Processes using Operando Nanoscopy (UPON) with project number 14205 (B2), which is (partly) financed by the Dutch Research Council (NWO). T.R. de Kruijff, E. Grafhorst, J. Li, M. Ahmadi and Z. Yue who were involved in UPON projects A1 and A2 are also acknowledged for developing the TEM holders and liquid chips in Prof. Zandbergen's group.

References

1. J.R. Scully, in *Future Frontiers in Corrosion Science and Engineering, Part I*, ed.NACE International, 2018).
2. J.R. Scully, in *Future Frontiers in Corrosion Science and Engineering, Part Ii: Managing the Many Stages of Corrosion*, ed.NACE International, 2019).
3. V. Maurice, P. Marcus, *Progress in Materials Science* 95, (2018): p. 132-171.
4. R. Parvizi, M.Y. Tan, A.E. Hughes, in *Recent Insights into Corrosion Initiation at the Nanoscale*, ed.Elsevier, 2018), p. 525-551.
5. F. Renner, A. Stierle, H. Dosch, D. Kolb, T.-L. Lee, J. Zegenhagen, *Nature* 439, 7077 (2006): p. 707.
6. N. Badwe, X. Chen, D.K. Schreiber, M.J. Olszta, N.R. Overman, E. Karasz, A. Tse, S.M. Bruemmer, K. Sieradzki, *Nature materials* 17, 10 (2018): p. 887-893.
7. M. Bettayeb, V. Maurice, L.H. Klein, L. Lapeire, K. Verbeken, P. Marcus, *Electrochimica Acta*, (2019):
8. R. Parvizi, A.E. Hughes, M.Y. Tan, R.K. Marceau, M. Forsyth, P. Cizek, A.M. Glenn, *Corrosion Science* 116, (2017): p. 98-109.
9. D.B. Williams, C.B. Carter, in *The Transmission Electron Microscope*, ed.Springer, 1996), p. 3-17.
10. E. Hamada, K. Yamada, M. Nagoshi, N. Makiishi, K. Sato, T. Ishii, K. Fukuda, S. Ishikawa, T. Ujiro, *Corrosion Science* 52, 12 (2010): p. 3851-3854.
11. S. Malladi, Q. Xu, F. Tichelaar, H. Zandbergen, F. Hannour, J. Mol, H. Terryn, *Surface and Interface Analysis* 45, 10 (2013): p. 1619-1625.
12. K. Oh, S. Ahn, K. Eom, K. Jung, H. Kwon, *Corrosion Science* 79, (2014): p. 34-40.

13. R.P. Wei, C.-M. Liao, M. Gao, *Metallurgical and Materials Transactions A* 29, 4 (1998): p. 1153-1160.
14. B. Zhang, J. Wang, B. Wu, X. Guo, Y. Wang, D. Chen, Y. Zhang, K. Du, E. Oguzie, X. Ma, *Nature communications* 9, 1 (2018): p. 2559.
15. D. Sun, Y. Jiang, Q. Xiang, C. Zhong, J. Gong, L. Zhang, J. Li, *Materials and corrosion* 61, 2 (2010): p. 105-110.
16. Y. Zhou, Y. Wang, S. Zheng, B. Zhang, X. Ma, *Philosophical Magazine* 95, 22 (2015): p. 2365-2375.
17. S. Persaud, S. Ramamurthy, A. Korinek, G. Botton, R. Newman, *Corrosion Science* 106, (2016): p. 117-126.
18. S. Persaud, J. Smith, A. Korinek, G. Botton, R. Newman, *Corrosion Science* 106, (2016): p. 236-248.
19. S. Kairy, P. Rometsch, C. Davies, N. Birbilis, *Corrosion* 73, 1 (2016): p. 87-99.
20. S. Malladi, F. Tichelaar, Q. Xu, M. Wu, H. Terryn, J. Mol, F. Hannour, H. Zandbergen, *Corrosion Science* 69, (2013): p. 221-225.
21. B. Zhang, X. Ma, *Journal of Materials Science & Technology*, (2019):
22. B. Zhang, J. Wang, B. Wu, Y. Zhou, X. Ma, *Corrosion Science* 100, (2015): p. 295-305.
23. Y. Zhang, P. Gore, W. Rong, Y. Wu, Y. Yan, R. Zhang, L. Peng, J.-F. Nie, N. Birbilis, *Corrosion Science* 136, (2018): p. 106-118.
24. A. Glenn, A. Hughes, T. Muster, D. Lau, N. Wilson, A. Torpy, C. MacRae, J. Ward, *Journal of The Electrochemical Society* 160, 3 (2013): p. C119-C127.
25. N. De Jonge, F.M. Ross, *Nature nanotechnology* 6, 11 (2011): p. 695.
26. K.L. Klein, I.M. Anderson, N. De Jonge, *Journal of microscopy* 242, 2 (2011): p. 117-123.
27. H.-G. Liao, H. Zheng, *Annual review of physical chemistry* 67, (2016): p. 719-747.
28. M. Williamson, R. Tromp, P. Vereecken, R. Hull, F. Ross, *Nature materials* 2, 8 (2003): p. 532.
29. K. Jungjohann, C.B. Carter, in *In Situ and Operando*, ed.Springer, 2016), p. 17-80.
30. J.E. Evans, K.L. Jungjohann, N.D. Browning, I. Arslan, *Nano letters* 11, 7 (2011): p. 2809-2813.
31. M. Tanase, J. Winterstein, R. Sharma, V. Aksyuk, G. Holland, J.A. Liddle, *Microscopy and Microanalysis* 21, 6 (2015): p. 1629-1638.
32. E.R. White, S.B. Singer, V. Augustyn, W.A. Hubbard, M. Mecklenburg, B. Dunn, B.C. Regan, *Acs Nano* 6, 7 (2012): p. 6308-6317.
33. T. Xu, L. Sun, *Superlattices and Microstructures* 99, (2016): p. 24-34.
34. M.R. Hauwiller, X. Zhang, W.-I. Liang, C.-H. Chiu, Q. Zhang, W. Zheng, C. Ophus, E.M. Chan, C. Czarnik, M. Pan, *Nano letters* 18, 10 (2018): p. 6427-6433.
35. G. Burstein, C. Liu, R. Souto, S. Vines, *Corrosion Engineering, Science and Technology* 39, 1 (2004): p. 25-30.
36. N. Casillas, S. Charlebois, W.H. Smyrl, H.S. White, *Journal of the Electrochemical Society* 141, 3 (1994): p. 636-642.
37. G. Frankel, *Journal of the Electrochemical Society* 145, 6 (1998): p. 2186-2198.
38. Z. Szklarska-Smialowska, *Corrosion science* 41, 9 (1999): p. 1743-1767.
39. G.L. Song, A. Atrens, *Advanced engineering materials* 1, 1 (1999): p. 11-33.
40. F.M. Ross, in *Quantifying Electrochemical Processes Using Liquid Cell Tem*, ed. F.M. Ross, ed.(Cambridge: Cambridge University Press, 2016), p. 210-236.
41. B.L. Mehdi, J. Qian, E. Nasybulin, C. Park, D.A. Welch, R. Faller, H. Mehta, W.A. Henderson, W. Xu, C.M. Wang, *Nano letters* 15, 3 (2015): p. 2168-2173.
42. A. Radisic, P.M. Vereecken, J.B. Hannon, P.C. Searson, F.M. Ross, *Nano Letters* 6, 2 (2006): p. 238-242.
43. J.H. Park, N.M. Schneider, D.A. Steingart, H. Deligianni, S. Kodambaka, F.M. Ross, *Nano letters* 18, 2 (2018): p. 1093-1098.
44. M. Moayed, R. Newman, *Corrosion science* 48, 4 (2006): p. 1004-1018.
45. P. Pistorius, G. Burstein, *Philosophical Transactions of the Royal Society of London. Series A: Physical and Engineering Sciences* 341, 1662 (1992): p. 531-559.
46. S. Pride, J. Scully, J. Hudson, *Journal of the Electrochemical Society* 141, 11 (1994): p. 3028-3040.
47. G. Frankel, L. Stockert, F. Hunkeler, H. Boehni, *Corrosion* 43, 7 (1987): p. 429-436.
48. S. Virtanen, C. Curty, *Corrosion* 60, 7 (2004): p. 643-649.
49. Y. Tang, Y. Zuo, J. Wang, X. Zhao, B. Niu, B. Lin, *Corrosion Science* 80, (2014): p. 111-119.
50. N. Birbilis, R.G. Buchheit, *Journal of The Electrochemical Society* 152, 4 (2005): p. B140-B151.
51. N. Birbilis, Y. Zhu, S. Kairy, M. Glenn, J.-F. Nie, A. Morton, Y. Gonzalez-Garcia, H. Terryn, J. Mol, A. Hughes, *Corrosion Science* 113, (2016): p. 160-171.
52. L.R. Parent, E. Bakalis, M. Proetto, Y. Li, C. Park, F. Zerbetto, N.C. Gianneschi, *Accounts of chemical research* 51, 1 (2017): p. 3-11.
53. N. Hodnik, G. Dehm, K.J. Mayrhofer, *Accounts of chemical research* 49, 9 (2016): p. 2015-2022.
54. F.M. Ross, *Science* 350, 6267 (2015): p. aaa9886.
55. T.J. Woehl, K.L. Jungjohann, J.E. Evans, I. Arslan, W.D. Ristenpart, N.D. Browning, *Ultramicroscopy* 127, (2013): p. 53-63.
56. N. de Jonge, F.M. Ross, in *Past, Present, and Future Electron Microscopy of Liquid Specimens*, ed. F.M. Ross, ed.(Cambridge: Cambridge University Press, 2016), p. 3-34.
57. E. Jensen, K. Mølhave, in *Encapsulated Liquid Cells for Transmission Electron Microscopy*, ed. F.M. Ross, ed.(Cambridge: Cambridge University Press, 2016), p. 35-55.
58. A.J. Leenheer, J.P. Sullivan, M.J. Shaw, C.T. Harris, *Journal of Microelectromechanical Systems* 24, 4 (2015): p. 1061-1068.
59. M. Denoual, V. Menon, T. Sato, O. De Sagazan, A. Coleman, H. Fujita, *Measurement Science and Technology* 30, 1 (2018): p. 017001.
60. J. Yang, O. Paul, *Sensors and Actuators A: Physical* 97, (2002): p. 520-526.
61. T. Alan, J. Gaspar, O. Paul, H.W. Zandbergen, F. Creemer, P.M. Sarro, "Characterization of Ultrathin Membranes to Enable Tem Observation of Gas Reactions at High Pressures," ASME 2009 International Mechanical Engineering Congress and ExpositionAmerican Society of Mechanical Engineers, 2009), p. 327-331.
62. A. Erdamar, S. Malladi, F. Tichelaar, H. Zandbergen, in *Closed Cell Systems for in Situ Tem with Gas Environments Ranging from 0.1 to 5 Bar*, ed.Springer, 2016), p. 165-210.
63. N.M. Schneider, in *Electron Beam Effects in Liquid Cell Tem and Stem*, ed. F.M. Ross, ed.(Cambridge: Cambridge University Press, 2016), p. 140-163.
64. N. de Jonge, N.D. Browning, J.E. Evans, S.W. Chee, F.M. Ross, in *Resolution in Liquid Cell Experiments*, ed. F.M. Ross, ed.(Cambridge: Cambridge University Press, 2016), p. 164-188.
65. L.A. Giannuzzi, F.A. Stevie, *Micron* 30, 3 (1999): p. 197-204.

66. M. Schaffer, B. Schaffer, Q. Ramasse, *Ultramicroscopy* 114, (2012): p. 62-71.
67. J. Mayer, L.A. Giannuzzi, T. Kamino, J. Michael, *MRS bulletin* 32, 5 (2007): p. 400-407.
68. K.A. Unocic, M.J. Mills, G. Daehn, *Journal of microscopy* 240, 3 (2010): p. 227-238.
69. X.L. Zhong, S. Schilling, N.J. Zaluzec, M.G. Burke, *Microscopy and Microanalysis* 22, 6 (2016): p. 1350-1359.
70. X. Zhong, M. Burke, S. Schilling, S. Haigh, N. Zaluzec, *Microscopy and Microanalysis* 20, S3 (2014): p. 1514-1515.
71. S.-J. Lee, J.-J. Lai, *Journal of Materials Processing Technology* 140, 1-3 (2003): p. 206-210.
72. M. Yu, J. Yi, J. Liu, S. Li, G. Wu, L. Wu, *Journal of Wuhan University of Technology-Mater. Sci. Ed.* 26, 3 (2011): p. 469-477.
73. N. de Jonge, L. Houben, R.E. Dunin-Borkowski, F.M. Ross, *Nature Reviews Materials*, (2018): p. 1.
74. N. De Jonge, D.B. Peckys, G. Kremers, D. Piston, *Proceedings of the National Academy of Sciences* 106, 7 (2009): p. 2159-2164.
75. N.D. Browning, J.E. Evans, in *The Potential for Imaging Dynamic Processes in Liquids with High Temporal Resolution*, ed. F.M. Ross, ed.(Cambridge: Cambridge University Press, 2016), p. 456-475.
76. R. Ramachandra, H. Demers, N. de Jonge, *Microscopy and microanalysis* 19, 1 (2013): p. 93-101.
77. N. de Jonge, *Ultramicroscopy* 187, (2018): p. 113-125.
78. M.E. Holtz, Y. Yu, J. Gao, H.D. Abruña, D.A. Muller, *Microscopy and Microanalysis* 19, 4 (2013): p. 1027-1035.
79. R.F. Egerton, *Electron Energy-Loss Spectroscopy in the Electron Microscope*, Springer Science & Business Media, 2011).
80. J.M. Grogan, N.M. Schneider, F.M. Ross, H.H. Bau, *Nano letters* 14, 1 (2013): p. 359-364.
81. T. Woehl, P. Abellan, *Journal of microscopy* 265, 2 (2017): p. 135-147.
82. N.M. Schneider, M.M. Norton, B.J. Mendel, J.M. Grogan, F.M. Ross, H.H. Bau, *The Journal of Physical Chemistry C* 118, 38 (2014): p. 22373-22382.
83. P. Abellan, T. Woehl, L. Parent, N. Browning, J. Evans, I. Arslan, *Chemical Communications* 50, 38 (2014): p. 4873-4880.
84. T. Gupta, N.M. Schneider, J.H. Park, D. Steingart, F.M. Ross, *Nanoscale* 10, 16 (2018): p. 7702-7710.
85. B. Zaid, D. Saidi, A. Benzaid, S. Hadji, *Corrosion Science* 50, 7 (2008): p. 1841-1847.
86. N. Schiff, B. Grosgogeat, M. Lissac, F. Dalard, *Biomaterials* 23, 9 (2002): p. 1995-2002.
87. Y. Feng, K.-S. Siow, W.-K. Teo, K.-L. Tan, A.-K. Hsieh, *Corrosion* 53, 5 (1997): p. 389-398.
88. E. Atinault, V. De Waele, U. Schmidhammer, M. Fattahi, M. Mostafavi, *Chemical Physics Letters* 460, 4-6 (2008): p. 461-465.
89. S. Garcia, T. Markley, J. Mol, A. Hughes, *Corrosion Science* 69, (2013): p. 346-358.
90. A. Hughes, T. Markley, S. Garcia, J. Mol, *Corrosion Engineering, Science and Technology* 49, 8 (2014): p. 674-687.
91. K.A. Yasakau, M.L. Zheludkevich, S.V. Lamaka, M.G. Ferreira, *The Journal of Physical Chemistry B* 110, 11 (2006): p. 5515-5528.
92. M.S.A. Asghar, B.J. Inkson, G. Möbus, *ChemPhysChem* 18, 10 (2017): p. 1247-1251.
93. T.J. Woehl, J.E. Evans, I. Arslan, W.D. Ristenpart, N.D. Browning, *ACS nano* 6, 10 (2012): p. 8599-8610.
94. E. Fahrenkrug, D.H. Alsem, N. Salmon, S. Maldonado, *Journal of The Electrochemical Society* 164, 6 (2017): p. H358-H364.
95. S. Schilling, A. Janssen, N.J. Zaluzec, M.G. Burke, *Microscopy and Microanalysis* 23, 4 (2017): p. 741-750.
96. R.R. Unocic, R.L. Sacci, G.M. Brown, G.M. Veith, N.J. Dudney, K.L. More, F.S. Walden, D.S. Gardiner, J. Damiano, D.P. Nackashi, *Microscopy and Microanalysis* 20, 2 (2014): p. 452-461.
97. S. Malladi, C. Shen, Q. Xu, T. de Kruijff, E. Yücelen, F. Tichelaar, H. Zandbergen, *Chemical Communications* 49, 92 (2013): p. 10859-10861.
98. S.W. Chee, J.-H. Park, A. Pinkowitz, B. Engler, F.M. Ross, D. Duquette, R. Hull, *Microscopy and Microanalysis* 21, S3 (2015): p. 973-974.
99. S.W. Chee, D.J. Duquette, F.M. Ross, R. Hull, *Microscopy and Microanalysis* 20, 2 (2014): p. 462-468.
100. S.W. Chee, S.H. Pratt, K. Hattar, D. Duquette, F.M. Ross, R. Hull, *Chemical Communications* 51, 1 (2015): p. 168-171.
101. J.H. Park, T. Watanabe, A. Pinkowitz, D.J. Duquette, R. Hull, D.A. Steingart, F.M. Ross, *Microscopy and Microanalysis* 24, S1 (2018): p. 254-255.
102. D. Gross, J. Kacher, J. Key, K. Hattar, I.M. Robertson, *Processing, Properties, and Design of Advanced Ceramics and Composites II* 261, (2017): p. 329.
103. M.P. Ryan, D.E. Williams, R.J. Chater, B.M. Hutton, D.S. McPhail, *Nature* 415, 6873 (2002): p. 770.
104. Y. Tsutsumi, A. Nishikata, T. Tsuru, *Corrosion science* 49, 3 (2007): p. 1394-1407.
105. A. Chiba, I. Muto, Y. Sugawara, N. Hara, *Journal of The Electrochemical Society* 160, 10 (2013): p. C511-C520.
106. T.S.L. Wijesinghe, D.J. Blackwood, *Corrosion Science* 49, 4 (2007): p. 1755-1764.
107. R. Ke, R. Alkire, *Journal of the Electrochemical Society* 139, 6 (1992): p. 1573-1580.
108. R. Ke, R. Alkire, *Journal of the Electrochemical Society* 142, 12 (1995): p. 4056-4062.
109. N. Laycock, R. Newman, *Corrosion science* 40, 6 (1998): p. 887-902.
110. B. Brown, S.R. Parakala, S. Nesic, *CORROSION/2004, paper*, 04736 (2004):
111. W. Tait, *corrosion* 35, 7 (1979): p. 296-300.
112. S. Nešic, J. Postlethwaite, *Corrosion* 47, 8 (1991): p. 582-589.
113. W. Sun, S. Nesic, *CORROSION 2007*, (2007):
114. S. Nešić, *Corrosion science* 49, 12 (2007): p. 4308-4338.
115. S.C. Hayden, C. Chisholm, R.O. Grudt, J.A. Aguiar, W.M. Mook, P.G. Kotula, T.S. Pilyugina, D.C. Bufford, K. Hattar, T.J. Kucharski, *npj Materials Degradation* 3, 1 (2019): p. 17.

FIGURE CAPTIONS

FIGURE 1. Schematic view of a typical transmission electron microscope together with its analytical techniques; the specimen is being illuminated in Scanning TEM (STEM) mode. Thin samples can be fabricated out of a “region of interest” either by argon-ion milling of approx. 50-µm thick disks or using focus ion beam (FIB) and lift-out procedures. TEM holders are used to mount electron-transparent samples (specimens) for examinations. The specimens can directly be imaged down to atomic level either with a broad static beam (TEM mode) or a scanning electron probe of typical 0.1 – 0.5 nm (STEM mode). An Annular Dark Field (ADF) detector (a ring) or Bright Field (BF) detector (a disc) is used for STEM imaging. An Energy Dispersive Spectroscopy (EDS) detector is used to collect X rays from the sample where the electron beam is. In STEM mode, elemental maps can be generated with a spatial resolution down to the electron probe size. High Resolution TEM (HR-TEM) allows for direct imaging of atomic

arrangements in materials (phase contrast imaging). A Selected Area (SA) aperture can be inserted to collect diffraction patterns (DP) of different locations on a specimen. By collecting and analyzing the inelastic transmitted electrons, it is possible to acquire information about elemental distribution and thickness variation within the specimen through Energy Filtered TEM (EF-TEM). The electronic structure like bonding and valence state of different phases can be analyzed using Electron Energy Loss Spectroscopy (EELS).

FIGURE 2. (a) Schematic of bottom and top chip of a liquid cell for TEM. The Pt electrodes are patterned onto the chips to make electrochemical measurements in the liquid cell possible; counter electrode CE, reference electrode RE and working electrode WE. The rectangular membranes facilitate the alignment of the electron transparent windows when clamping them together. (b) A dedicated TEM holder with a specific tip to place the liquid cell (assembled bottom and top chips) and make electrical connections to the liquid cell. It consists of a tubing systems, conveying electrolyte to run into the liquid cell through the inlet. A pressure difference between the inlet and outlet is applied by injection and vacuum pumps to have a controlled flow through the liquid cell. (c) Cross-sectional sketch of the holder tip loaded with a liquid cell. The inlet and outlet tubes go the entire distance from the injection pump to the other side of the holder, where they are attached to a vacuum pump; redrawn from Erdamar et al., [62] with permission from Springer Nature. (d) Cross-sectional view of a liquid cell loaded with a thin sample being irradiated (herein STEM mode). The incident beam can deposit energy into water which triggers radiolysis. Flowing the liquid can be an effective way to refresh the affected liquid.

FIGURE 3. Steps to cut and attach a thin specimen to the liquid cell (a) Dark-field STEM image showing the electron-transparent region on an electropolished disk (bright area), (b) cutting around the periphery of the transparent region, with corner attachments still in place. (c) Attaching the micromanipulator to the area of interest to be freed by milling off supporting material, (d) positioning the specimen above the window, (e) cutting off the micromanipulator and welding the specimen to the liquid cell by organometallic Pt deposition. Reprinted from Zhong et al., [69] with permission from Cambridge University Press.

FIGURE 4. Top–bottom effect on resolution in TEM and STEM imaging modes. The specimen is an approx. 200-nm-thick piece of AA2024-T3 corroded in 0.01 M NaCl for 1 hr. Images were recorded with liquid cell filled up with 1 bar air at 300 kV. The windows gap was about 700 nm, estimated by EELS. The thickness of top and bottom membranes was 60 nm. In TEM mode, the objective aperture was inserted. In STEM mode, an annular dark filed (ADF) detector (camera length 185 mm) was used. (a) TEM image, the specimen at the entrance. (b) TEM image, the specimen at the exit. (c) STEM image, the specimen at the entrance. (d) STEM image, the specimen at the exit. Cross-sectional schematics illustrate the geometries applied. Unpublished data.

FIGURE 5. (a) Schematic cross-section of a liquid cell placed in vacuum, showing bulging of the membranes which gives rise to a location-dependent liquid thickness. Therefore, TEM lamellae should be placed close to the edge of the window where bulging is minimum. (b) Maximum resolution versus thickness of water in TEM and STEM. The resolution is theoretically calculated for typical instrument parameters at 200 keV to image Au nanoparticles at the bottom of a layer of water for TEM, and at the top of the layer for STEM. Adapted from De Jonge and Ross [25] with permission from Springer Nature.

FIGURE 6. Influence of initial pH prior to irradiation and dose rate on steady state pH of the radiated region. The values are theoretically calculated for de-aerated water. The gray per second (Gy/s) is defined as the absorption of one joule per kilogram of matter per unit time. Reprinted from Schneider et al., [82] with permission from American Chemical Society.

FIGURE 7. Schematic top-view of a three-electrode configuration patterned on the chip. The working electrode (WE) is normally made of Pt or glassy carbon whereas the reference (RE) and counter (CE) electrodes are Pt. The similar configuration has been used for the experiments shown below. (b) Effect of electron beam on open circuit potential of a Pt electrode in aerated distilled water. (c) In-situ open circuit potential measurement of an austenitic stainless steel connected to a Pt electrode in 0.001M H_2SO_4. (a-c) are reprinted from Schilling et al., [95] with permission from Cambridge University Press. (d) Cyclic voltammetry of the $[Fe(CN)_6]^{4-}/Fe(CN)_6]^{3-}$ redox couple with the STEM beam on and beam off. STEM imaging has been done at 300 keV, giving electron dose of (154 e^-/nm^2 s). (e) Effect of flow rate on Nyquist plot of $[Fe(CN)_6]$ acquired with a glassy carbon WE at the constant potential of 0 V. (d, e) are reprinted from Unocic et al., [96] with permission from Cambridge University Press.

FIGURE 8. (a-f) Time-resolved TEM images showing preferential dissolution of small grains, leaving the adjacent grown gain isolated. Reprinted from Gross et al., [102] with permission from John Wiley and Sons. (d) Polarization curve of an Al thin film (from -200 mV to 500 mV) in 0.1 M Na_2SO_4 and 0.001 M NaCl solution. (g-j) Snapshots of microstructural evolutions at different points of the curve revealing the dissolution of single grains (indicated with white arrows). Note that this is the second time that the sample has been polarized in the solution. Reprinted from Chee et al., [98] with permission from Cambridge University Press.

FIGURE 9. Bright filed STEM images together with EDS maps of type 304 stainless steel revealing dissolution of a MnS inclusion after 24 h in flowing deionized H_2O at the room temperature. Adapted from Schilling et al., [95] with permission from Cambridge University Press.

FIGURE 10. (a) Schematic of the liquid cell loaded with a 1018 steel lamella. (b) Bright field STEM image of a region that was microstructurally and chemically characterized before exposure to 2.78 µM Na_2SO_4 solution. A cementite grain inclusion fully confined by a ferrite matrix and different triple junctions TJ1, TJ2, and TJ3 indicated by white arrows. (c–f) Time-resolved bright field STEM images of the region during exposure to the flowing solution. Having initiated at TJ1, localized corrosion took place in the 1018 steel sample at the phase boundary between ferrite and cementite. (g-i) Concurrent occurrence of uniform corrosion revealed by bright field STEM micrograph of the lamella (g) before, and (h) after 1025 min exposure. (i) Energy filtered TEM to relatively map the thickness of the corroded specimen. Reproduced from Hayden et al., [115] with permission from Springer Nature. The images were originally published as parts of three distinct figures.

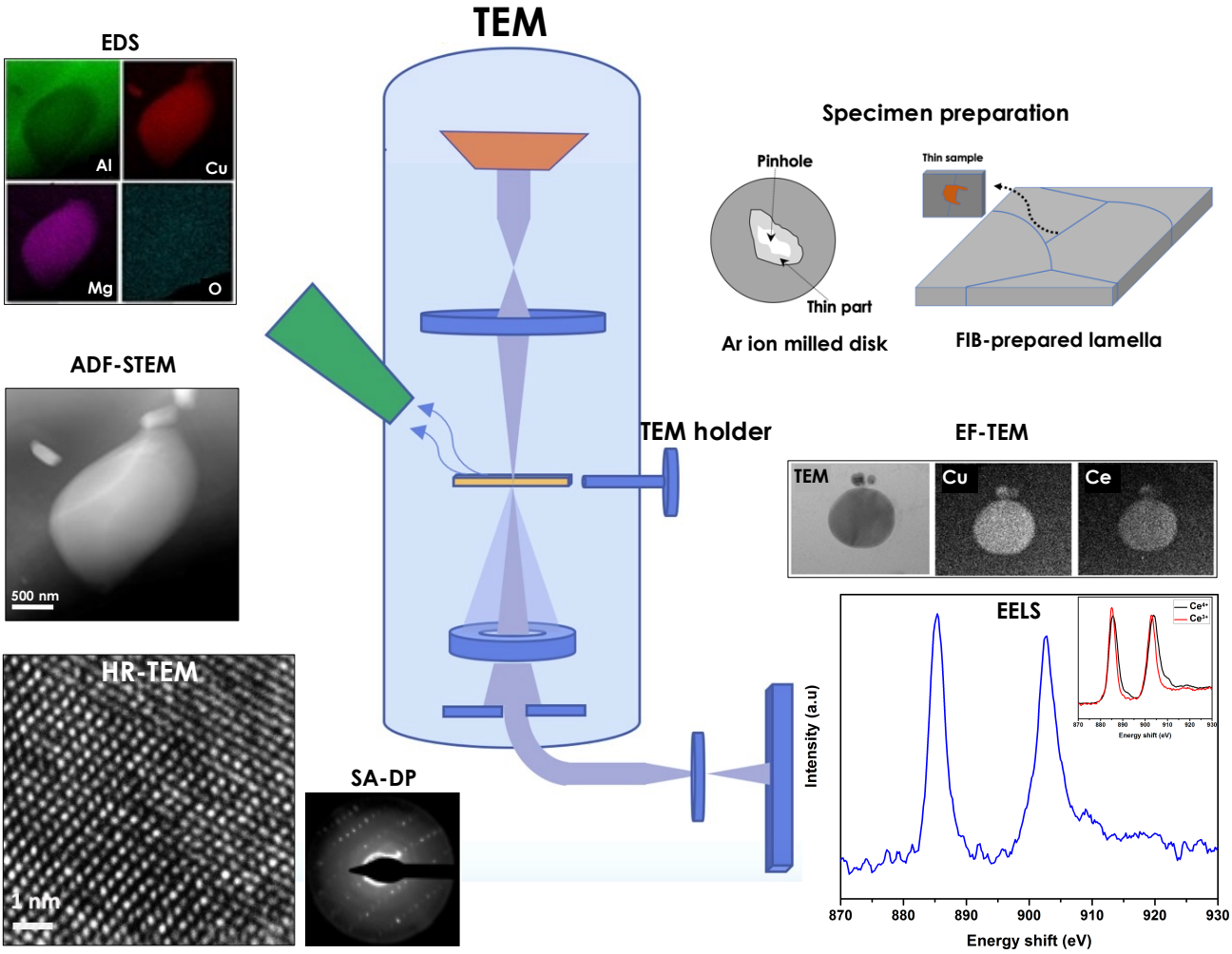

Fig. 1, Schematic view of a typical transmission electron microscope together with its analytical techniques; the specimen is being illuminated in Scanning TEM (STEM) mode. Thin samples can be fabricated out of a "region of interest" either by argon-ion milling of approx. 50-µm thick disks or using focus ion beam (FIB) and lift-out procedures. TEM holders are used to mount electron-transparent samples (specimens) for examinations. The specimens can directly be imaged down to atomic level either with a broad static beam (TEM mode) or a scanning electron probe of typical 0.1 – 0.5 nm (STEM mode). An Annular Dark Field (ADF) detector (a ring) or Bright Field (BF) detector (a disc) is used for STEM imaging. An Energy Dispersive Spectroscopy (EDS) detector is used to collect X rays from the sample where the electron beam is. In STEM mode, elemental maps can be generated with a spatial resolution down to the electron probe size. High Resolution TEM (HR-TEM) allows for direct imaging of atomic arrangements in materials (phase contrast imaging). A Selected Area (SA) aperture can be inserted to collect diffraction patterns (DP) of different locations on a specimen. By collecting and analyzing the inelastic transmitted electrons, it is possible to acquire information about elemental distribution and thickness variation within the specimen through Energy Filtered TEM (EF-TEM). The electronic structure like bonding and valence state of different phases can be analyzed using Electron Energy Loss Spectroscopy (EELS).

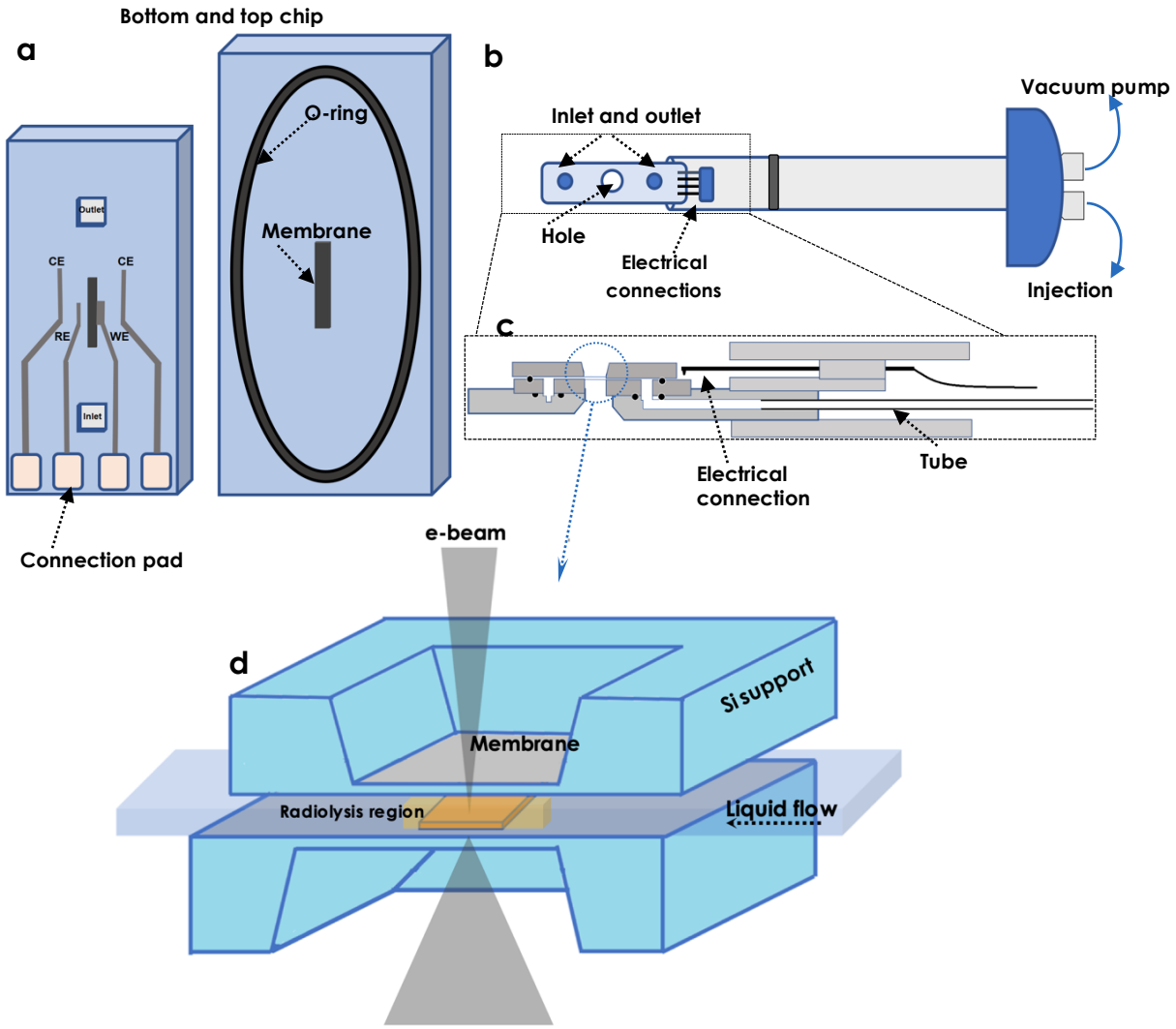

Fig. 2, (a) Schematic of bottom and top chip of a liquid cell for TEM. The Pt electrodes are patterned onto the chips to make electrochemical measurements in the liquid cell possible; counter electrode CE, reference electrode RE and working electrode WE. The rectangular membranes facilitate the alignment of the electron transparent windows when clamping them together. (b) A dedicated TEM holder with a specific tip to place the liquid cell (assembled bottom and top chips) and make electrical connections to the liquid cell. It consists of a tubing systems, conveying electrolyte to run into the liquid cell through the inlet. A pressure difference between the inlet and outlet is applied by injection and vacuum pumps to have a controlled flow through the liquid cell. (c) Cross-sectional sketch of the holder tip loaded with a liquid cell. The inlet and outlet tubes go the entire distance from the injection pump to the other side of the holder, where they are attached to a vacuum pump; redrawn from Erdamar et al., [62] with permission from Springer Nature. (d) Cross-sectional view of a liquid cell loaded with a thin sample being irradiated (herein STEM mode). The incident beam can deposit energy into water which triggers radiolysis. Flowing the liquid can be an effective way to refresh the affected liquid.

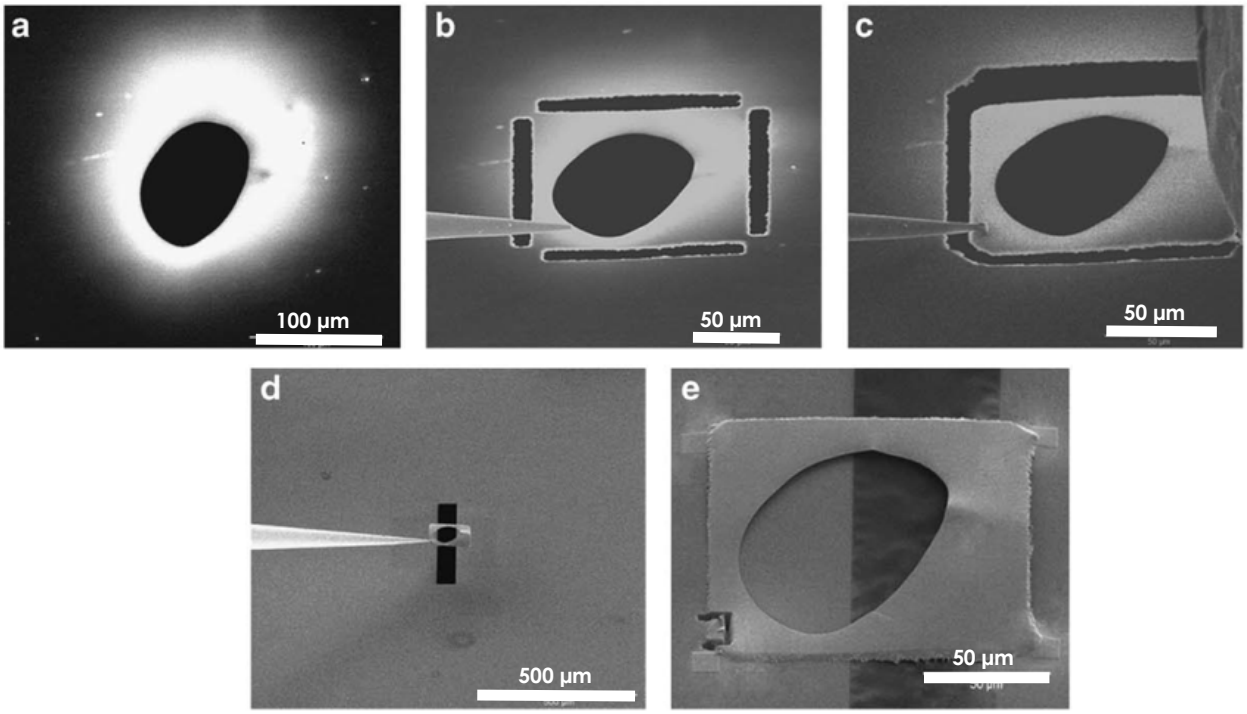

Fig. 3. Steps to cut and attach a thin specimen to the liquid cell (a) Dark-field STEM image showing the electron-transparent region on an electropolished disk (bright area), (b) cutting around the periphery of the transparent region, with corner attachments still in place. (c) Attaching the micromanipulator to the area of interest to be freed by milling off supporting material, (d) positioning the specimen above the window, (e) cutting off the micromanipulator and welding the specimen to the liquid cell by organometallic Pt deposition. Reprinted from Zhong et al., [69] with permission from Cambridge University Press.

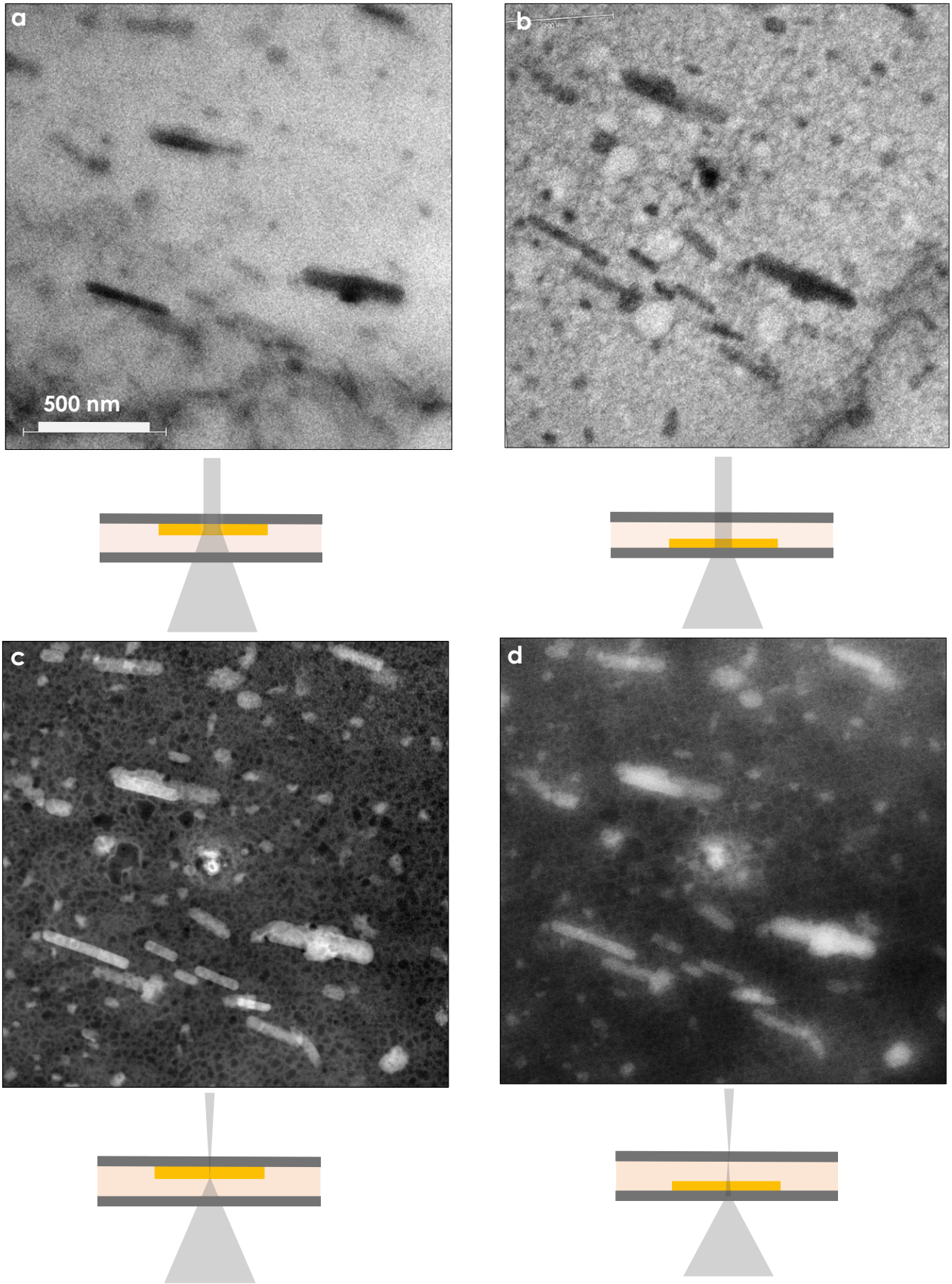
a
500 nm
b
c
d

Fig. 4, Top–bottom effect on resolution in TEM and STEM imaging modes. The specimen is an approx. 200-nm-thick piece of AA2024-T3 corroded in 0.01 M NaCl for 1 hr. Images were recorded with liquid cell filled up with 1 bar air at 300 kV. The windows gap was about 700 nm, estimated by EELS. The thickness of top and bottom membranes was 60 nm. In TEM mode, the objective aperture was inserted. In STEM mode, an annular dark filed (ADF) detector (Camera length 185 mm) was used. (a) TEM image, the specimen at the entrance. (b) TEM image, the specimen at the exit. (c) STEM image, the specimen at the entrance. (d) STEM image, the specimen at the exit. Cross-sectional schematics illustrate the geometries applied. Unpublished data.

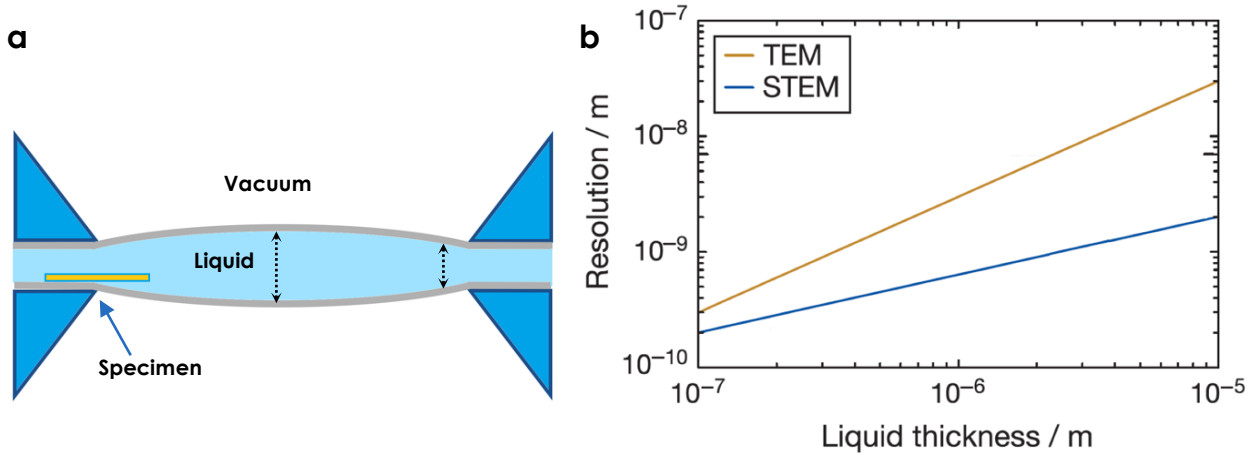

Fig. 5, (a) Schematic cross-section of a liquid cell placed in vacuum, showing bulging of the membranes which gives rise to a location-dependent liquid thickness. Therefore, TEM lamellae should be placed close to the edge of the window where bulging is minimum. (b) Maximum resolution versus thickness of water in TEM and STEM. The resolution is theoretically calculated for typical instrument parameters at 200 keV to image Au nanoparticles at the bottom of a layer of water for TEM, and at the top of the layer for STEM. Adapted from De Jonge and Ross [25] with permission from Springer Nature.

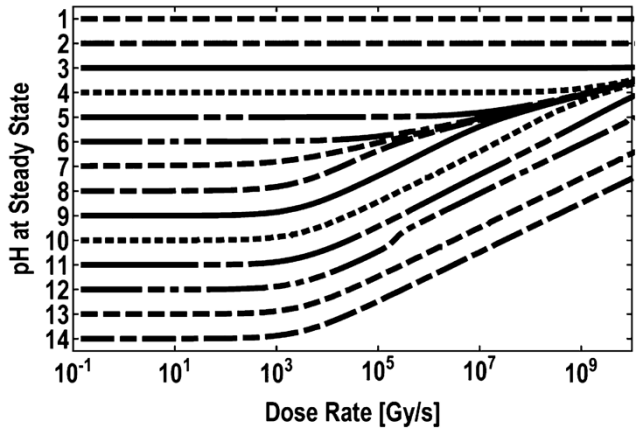

Fig. 6, Influence of initial pH prior to irradiation and dose rate on steady state pH of the radiated region. The values are theoretically calculated for de-aerated water. The gray per second (Gy/s) is defined as the absorption of one joule per kilogram of matter per unit time. Reprinted from Schneider et al., [82] with permission from American Chemical Society.

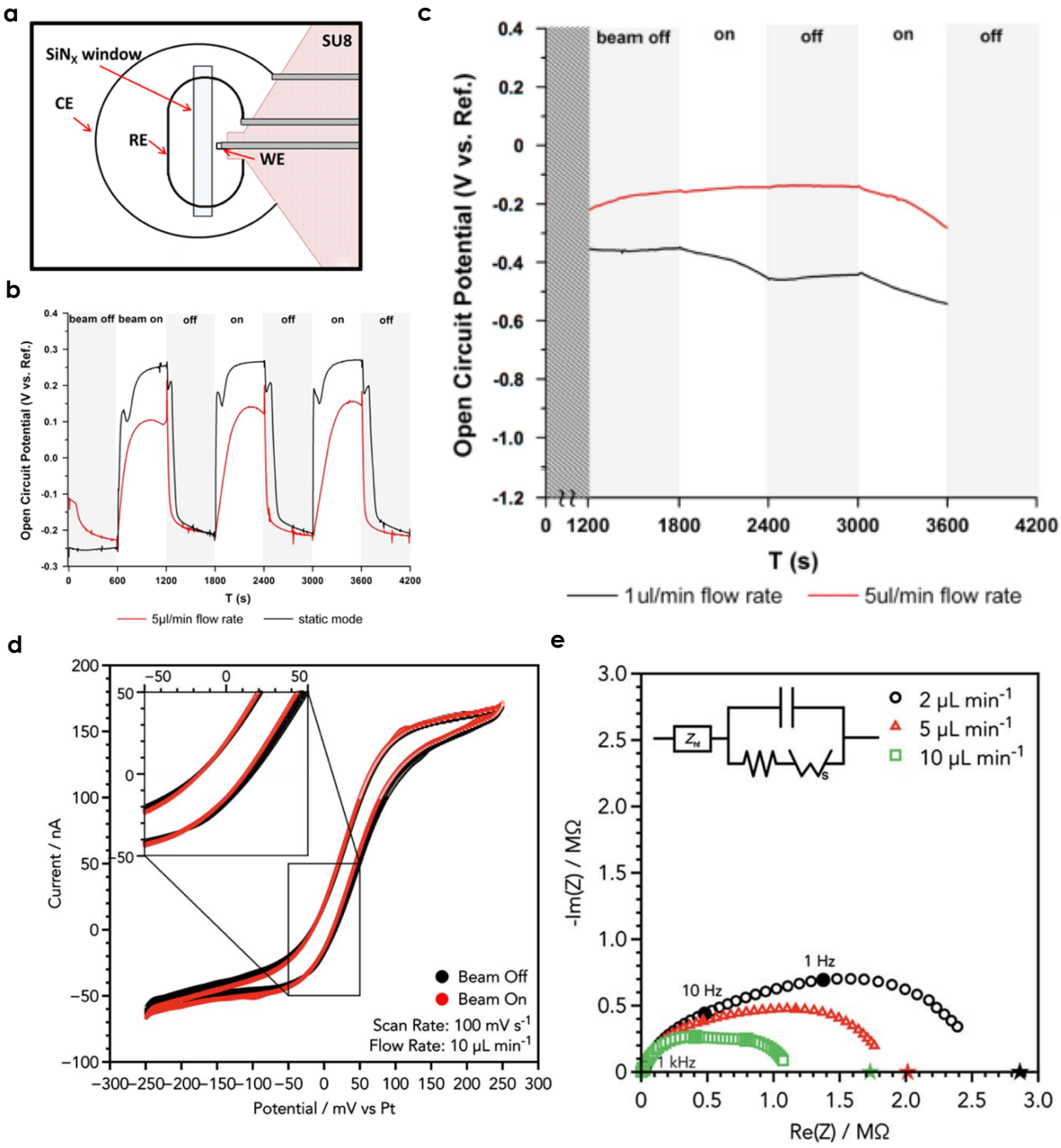

Fig. 7, Schematic top-view of a three-electrode configuration patterned on the chip. The working electrode (WE) is normally made of Pt or glassy carbon whereas the reference (RE) and counter (CE) electrodes are Pt. The similar configuration has been used for the experiments shown below. (b) Effect of electron beam on open circuit potential of a Pt electrode in aerated distilled water. (c) In-situ open circuit potential measurement of an austenitic stainless steel connected to a Pt electrode in 0.001M H_2SO_4. (a-c) are reprinted from Schilling et al., [95] with permission from Cambridge University Press. (d) Cyclic voltammetry of the $[Fe(CN)_6]^{4-}/Fe(CN)_6]^{3-}$ redox couple with the STEM beam on and beam off. STEM imaging has been done at 300 keV, giving electron dose of (154 e^-/nm^2 s). (e) Effect of flow rate on Nyquist plot of $[Fe(CN)_6]$ acquired with a glassy carbon WE at the constant potential of 0 V. (d, e) are reprinted from Unocic et al., [96] with permission from Cambridge University Press.

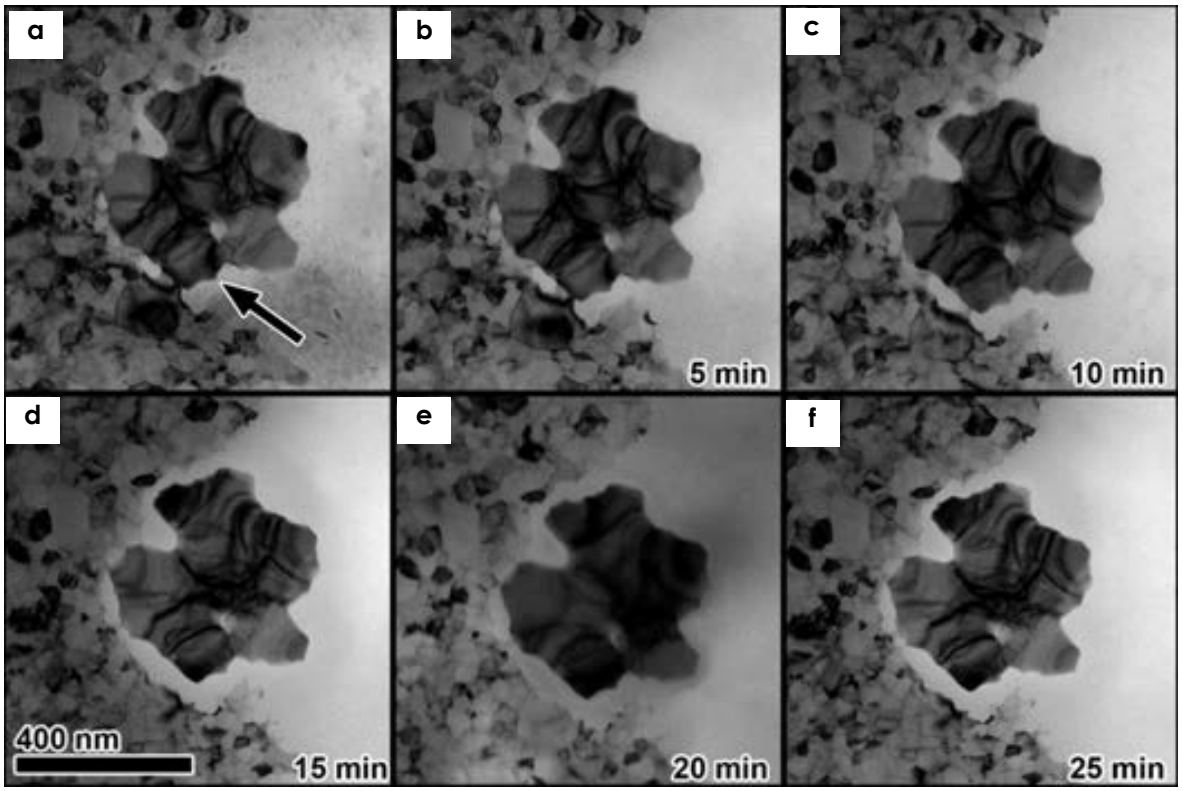
a
b
c
5 min
10 min
d
e
f
400 nm
15 min
20 min
25 min

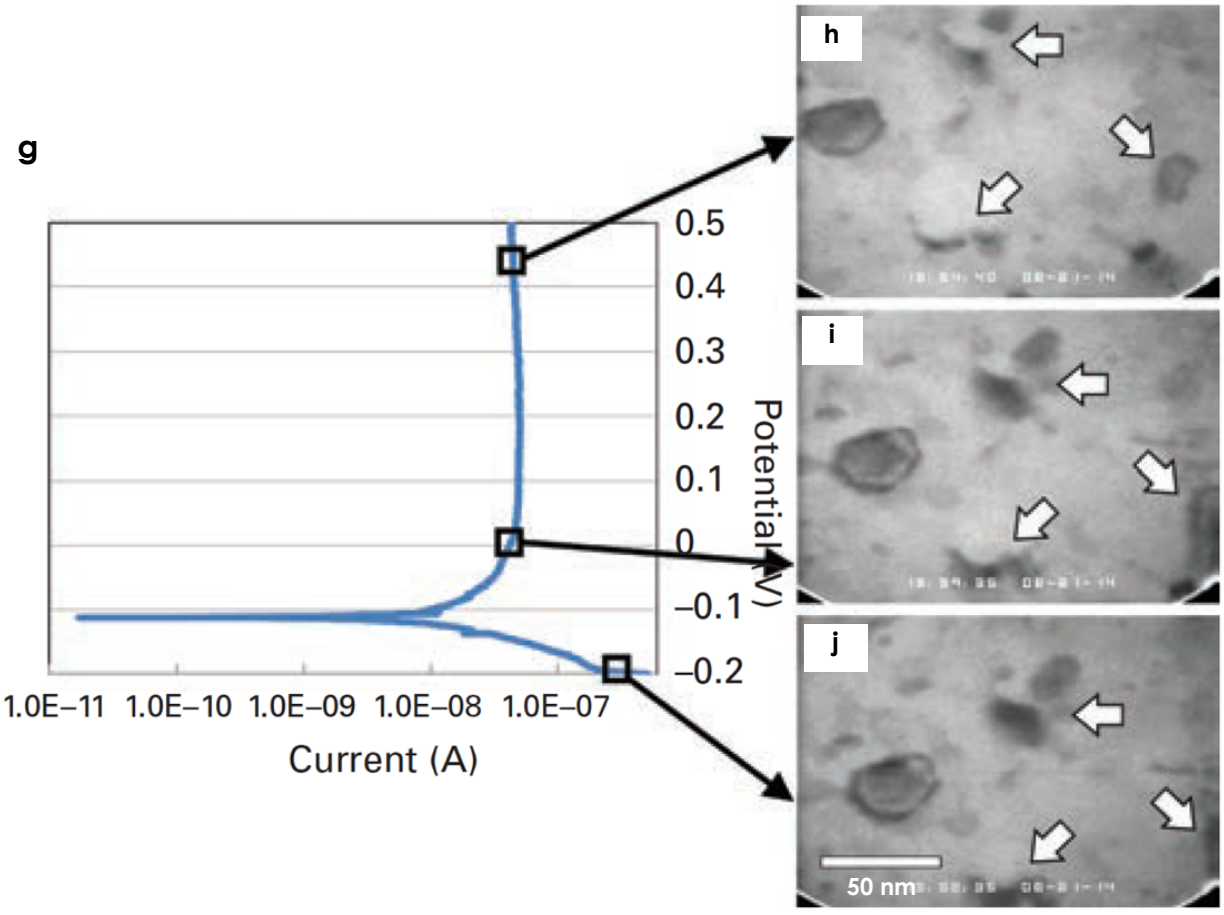
g
0.5
0.4
0.3
0.2
0.1
0
−0.1
−0.2
Potential (V)
1.0E−11
1.0E−10
1.0E−09
1.0E−08
1.0E−07
Current (A)
h
i
j
50 nm

Fig. 8, (a-f) Time-resolved TEM images showing preferential dissolution of small grains, leaving the adjacent grown gain isolated. Reprinted from Gross et al., [102] with permission from John Wiley and Sons. (d) Polarization curve of an Al thin film (from -200 mV to 500 mV) in 0.1 M Na_2SO_4 and 0.001 M NaCl solution. (g-j) Snapshots of microstructural evolutions at different points of the curve revealing the dissolution of single grains (indicated with white arrows). Note that this is the second time that the sample has been polarized in the solution. Reprinted from Chee et al., [98] with permission from Cambridge University Press.

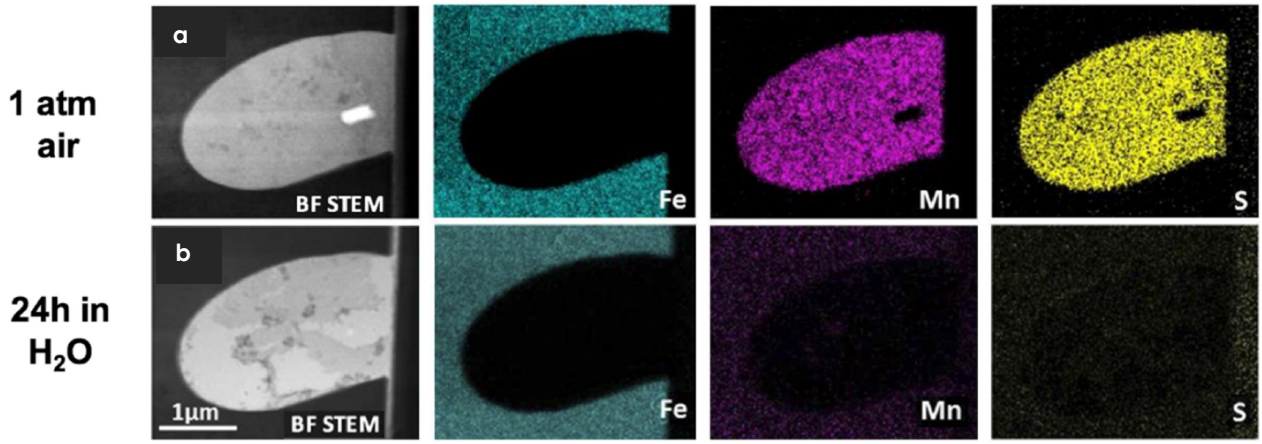

Fig. 9, Bright filed STEM images together with EDS maps of type 304 stainless steel revealing dissolution of a MnS inclusion after 24 h in flowing deionized H_2O at the room temperature. Adapted from Schilling et al., [95] with permission from Cambridge University Press.

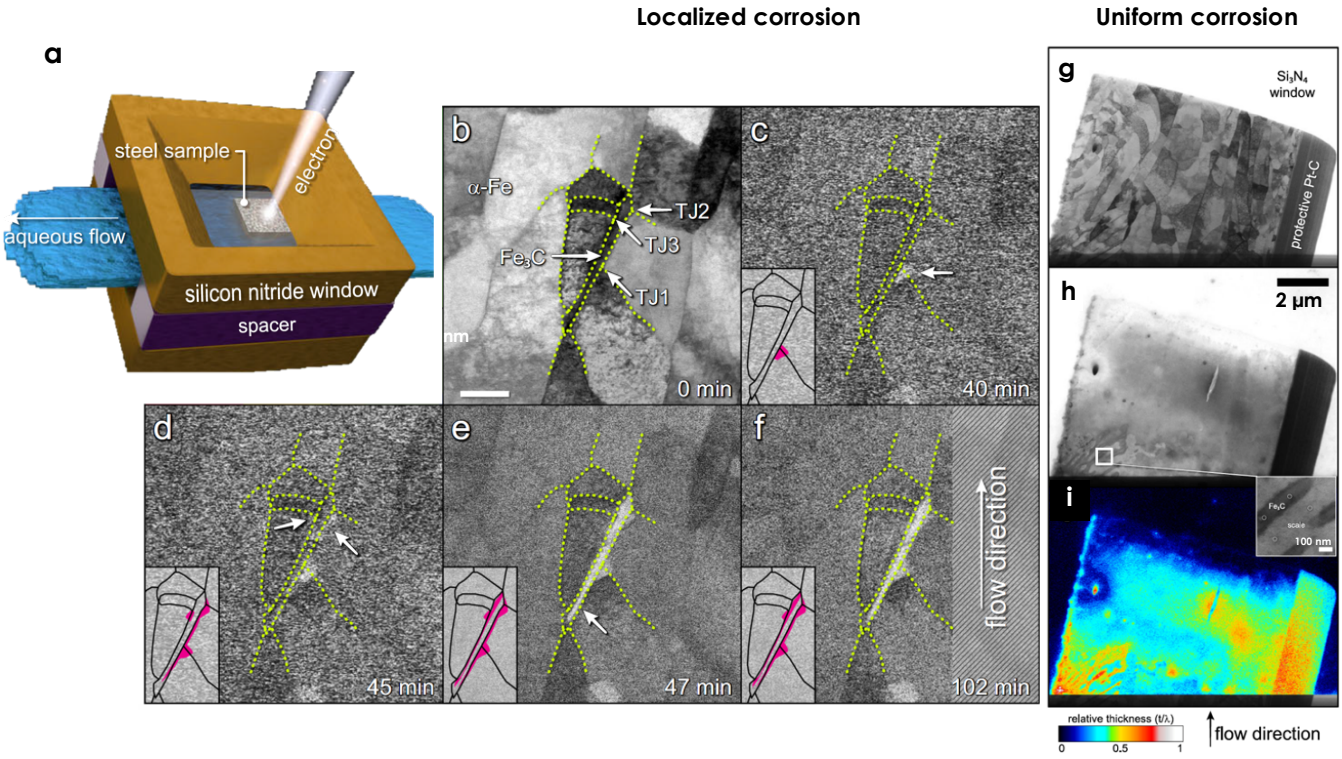

Fig. 10, (a) Schematic of the liquid cell loaded with a 1018 steel lamella. (b) Bright field STEM image of a region that was microstructurally and chemically characterized before exposure to 2.78 µM Na_2SO_4 solution. A cementite grain inclusion fully confined by a ferrite matrix and different triple junctions TJ1, TJ2, and TJ3 indicated by white arrows. (c–f) Time-resolved bright field STEM images of the region during exposure to the flowing solution. Having initiated at TJ1, localized corrosion took place in the 1018 steel sample at the phase boundary between ferrite and cementite. (g-i) Concurrent occurrence of uniform corrosion revealed by bright field STEM micrograph of the lamella (g) before, and (h) after 1025 min exposure. (i) Energy filtered TEM to relatively map the thickness of the corroded specimen. Reproduced from Hayden et al., [115] with permission from Springer Nature. The images were originally published as parts of three distinct figures.